Research Article

Journal of Environmental Nanotechnology

Development of MgO-reinforced Chitosan–CMC/ZnO Nanocomposite Films for Photocatalytic and Antimicrobial Applications

Anju Rani[1], Dhananjay Bhaurao Awachat[2], Manish S. Deshmukh[3], P. Satishkumar[4], Nischal P Mungle[5] and R. Prakash[6*]

[1]Department of Physics, School of Engineering and Technology, CGC University, Mohali, PB, India
[2]Department of Civil Engineering, K D K College of Engineering, Nagpur, MH, India
[3]Department of Mechanical Engineering, AISSMS College of Engineering, Pune, MH, India
[4]Department of Mechanical Engineering, Rathinam Technical Campus, Coimbatore, TN, India
[5]Department of Mechanical Engineering, Yeshawantrao Chavan College of Engineering, Wanadongari, Nagpur, MH, India
[6]Department of Science and Humanities, Rathinam Technical Campus, Coimbatore, TN, India
Received: 29.07.2026 Accepted: 31.08.2026 Published: xx.xx.xxxx
*prakashr2508@gmail.com

ABSTRACT

Chitosan–carboxymethyl cellulose/ZnO–MgO (Chitosan–CMC/ZnO–MgO) nanocomposite films were fabricated and evaluated for their thermal, structural, dielectric, mechanical, photocatalytic, interfacial, and antimicrobial characteristics. FT-IR showed interactions between polymer chains and incorporated nanoparticles, while SEM indicated relatively uniform particle dispersion throughout the matrix. XRD patterns verified the crystalline phases of magnesium oxide (MgO) and zinc oxide (ZnO), including the characteristic ZnO (101) reflection. Increasing the MgO concentration enhanced the thermal resistance of the films. Kissinger calculations showed that the activation energy (E_a) increased from 86 kJ/mol for the MgO-free film to 122 kJ/mol for the 3% MgO formulation. DSC measurements similarly revealed a rise in the glass-transition temperature (T_g) from 98.5 °C to 117 °C. Tensile strength improved from 28.6 MPa to 51.6 MPa, while Shore A hardness increased from 41.8 to 62.7. MgO incorporation also increased the dielectric constant. Surface wettability decreased, as demonstrated by the increase in the water contact angle from 71.26° to 93.17°. Under UV irradiation, crystal violet degradation increased from approximately 25% for the MgO-free film to 51% for the 3% MgO film. The same formulation generated inhibition zones of 15.28, 14.39, and 16.12 mm against *C. albicans, E. coli,* and *S. aureus*. Overall, MgO incorporation improved mechanical performance, enhanced photocatalytic efficiency, and showed promising preliminary antimicrobial activity. The developed films therefore offer potential for environmental treatment and antimicrobial surface applications. Nevertheless, before considering biomedical use, researchers must investigate their biocompatibility, cytotoxicity, long-term stability, and nanoparticle release.

Keywords: Antimicrobial activity; Activation energy; Thermal resistance; UV irradiation; Mechanical behavior.

1. INTRODUCTION

The rapid increase in plastic waste and environmental pollution has intensified the demand for biodegradable multifunctional materials that can replace conventional petroleum-based polymers in environmental, food packaging, and biomedical applications. Among naturally derived biopolymers, chitosan (CS) and carboxymethyl cellulose (CMC) have attracted considerable attention owing to biocompatibility, biodegradability, excellent film-forming ability, non-toxicity, and abundant hydroxyl and amino functional groups. Nevertheless, their practical applications remain limited by relatively poor mechanical strength, low thermal stability, insufficient antimicrobial activity, and limited photocatalytic performance. Consequently, incorporating functional metal oxide nanoparticles has emerged as an effective strategy to improve the structural integrity and multifunctionality of biodegradable polymer films.

Green synthesis has become an environmentally sustainable approach for preparing metal oxide nanoparticles because plant-derived phytochemicals simultaneously act as stabilizing and reducing agents. Green chitosan/polyvinyl alcohol (CS/PVA) nanocomposite films incorporating 2–8 wt.% L-glutamic acid-functionalized ZnO nanoparticles (ZnO NPs) synthesized using mango peel ash extract exhibited enhanced mechanical, barrier, antioxidant, antibacterial, and photocatalytic properties, achieving 98% methylene blue degradation within 120 min under sunlight, demonstrating their suitability for food packaging and environmental remediation (Kamanna *et al.* 2023). Similarly, L-glutamic acid-coated ZnO NPs synthesized using guava leaf extract increased the particle size from

25.32 to 41.88 nm, improved the zeta potential from −9.05 to −18.6 mV, and exhibited IC_{50} values of 40.43 µg/mL against HeLa cells, 37.20 µg/mL against A549 cells, and 44.23 µg/mL against MCF-7 cells, confirming that surface functionalization significantly enhances nanoparticle compatibility and biological activity (Huong *et al.* 2025).

ZnO-based nanocomposite coatings show strong potential for active food preservation. A ZnO–TiO_2–Bi_2WO_6 ternary heterojunction incorporated into carboxymethyl chitosan edible films exhibited >99.99% antibacterial efficiency against *Escherichia coli* and *Staphylococcus aureus* after 24 h, while photocatalytic ethylene degradation effectively prolonged banana storage at 30 °C and 90% relative humidity (Ma *et al.* 2024). Likewise, chitosan-conjugated *Punica granatum*-derived ZnO nanocomposite films containing 7.5% nanoparticles extended the shelf life of cherry tomatoes from 4 to 16 days and Indian anchovy from 4 to 9 days, while providing excellent antioxidant and antibacterial performance (Sangodkar *et al.* 2026). Photocatalytically active ZnO-containing chitosan films have also demonstrated simultaneous pollutant degradation and antimicrobial activity. Chitosan films reinforced with ZnO and reduced graphene oxide achieved 97% malachite green degradation within 120 min under visible light and produced inhibition zones of 9.32 ± 0.27 mm against *E. coli* and 10.23 ± 0.25 mm against *S. aureus* (Pham *et al.* 2025). Similarly, optimized chitosan films containing 0.2% ZnO exhibited excellent antimicrobial activity, while films reinforced with 1–3% ZnO achieved 87.94% methylene blue degradation with pseudo-first-order rate constants ranging from 55.1×10^{-4} to 81.3×10^{-4} h^{-1}, demonstrating the multifunctionality of ZnO-based biodegradable films (Karabaş *et al.* 2025).

Hybrid nanostructures have further improved the functionality of chitosan composites. Sodium alginate/chitosan nanocomposite films containing 1.5 wt.% CuO and 0.5 wt.% ZnO NPs exhibited >60% bacterial inhibition in the dark and >90% inhibition under light irradiation through reactive oxygen species (ROS) generation and membrane disruption (Guan *et al.* 2021). Besides ZnO, magnesium oxide (MgO) nanoparticles have attracted increasing interest because of their excellent chemical stability, thermal resistance, antimicrobial activity, and photocatalytic performance. Microporous chitosan/gelatin films reinforced with 1 wt.% MgO NPs exhibited pore diameters of 73–103 µm, porosity of 57–78%, and significantly improved bioactivity, antimicrobial activity, controlled biodegradation, and cell migration for wound healing applications (Attayil *et al.* 2022). Similarly, bio-based chitosan/rice husk nanocellulose films reinforced with nano-MgO exhibited a crystallinity of 84.9%, enhanced thermal stability up to 265 °C, and achieved 70.16% 2,2-diphenyl-1-picrylhydrazyl (DPPH) antioxidant activity, demonstrating their suitability for sustainable food packaging uses (Valsalan *et al.* 2026).

A comprehensive review further highlighted that MgO NP-reinforced biodegradable films significantly improve mechanical strength, water-vapor barrier properties, UV shielding, thermal stability, antimicrobial activity, and shelf-life extension, establishing MgO as one of the most promising multifunctional nanofillers for sustainable polymer packaging systems (Yang *et al.* 2024). Furthermore, green-synthesized ZnO NPs prepared using guava leaf extract exhibited a crystallite size of 25.08 nm, an optical band gap of 3.33 eV, and excellent antibacterial activity while maintaining only 3.2% hemolysis at 500 µg/mL, demonstrating the safety and effectiveness of plant-mediated ZnO NPs for biomedical and environmental applications (Al-Odayni *et al.* 2024). Researchers have also successfully incorporated natural bioactive compounds into biodegradable films to improve active food-packaging performance. Tea polyphenol-loaded chitosan NPs incorporated into CMC/potato starch films exhibited sustained release following the Weibull model (R^2 = 0.9742–0.9867) and effectively preserved refrigerated pork at 4 °C by suppressing microbial growth and oxidative deterioration (Li *et al.* 2026). Likewise, CMC nanocomposite films containing nano-encapsulated pomegranate flavonoids with a particle size of 232 nm successfully extended the shelf life of beef and poultry meat to 12 days through enhanced antimicrobial and antioxidant activities (Khalid *et al.* 2024).

The development of intelligent packaging systems has further expanded the applications of chitosan and CMC-based composites. A multifunctional CMC/chitosan composite film containing anthocyanins and graphene nanoplatelets achieved >98% antimicrobial efficiency within 10 min of light irradiation while simultaneously providing pH-responsive colorimetric freshness monitoring for shrimp preservation (Huang *et al.* 2026). Apart from ZnO and MgO, several metal oxide NPs have demonstrated outstanding multifunctional performance. Cu-doped SnO_2 NPs containing 15 wt.% Cu achieved 95% crystal violet degradation within 105 min under sunlight while improving dielectric properties through efficient charge separation (Bisht *et al.* 2025). Green-synthesized CeO_2 NPs deposited on banyan aerial root fiber composites improved tensile strength from 6.2 to 8.4 MPa, achieved a flexural strength of 18.9 MPa, and reduced water absorption to 2.63 ± 0.19%, demonstrating the effectiveness of green metal oxide nanocomposites for sustainable structural applications (Jachak *et al.* 2026).

Despite these advances, most reported chitosan-based nanocomposites incorporate a single biopolymer matrix combined with either ZnO or MgO alone, and studies exploring CS blended with CMC as a dual-biopolymer matrix remain scarce. Furthermore, while

ZnO and MgO have each individually demonstrated strong antimicrobial and photocatalytic performance, their combined incorporation into a single chitosan-based film system to achieve synergistic dual-nanoparticle reinforcement has not been adequately explored. Existing hybrid systems such as CuO–ZnO or ZnO–TiO_2–Bi_2WO_6 rely on transition-metal or multi-component heterojunctions, whereas a simpler, cost-effective ZnO–MgO combination within a CS–CMC matrix offering simultaneous mechanical, thermal, electrical, and dual-functional (photocatalytic and antimicrobial) enhancement has not been reported. This study addresses this gap by developing a CS–CMC film reinforced with green-synthesized ZnO and MgO NPs. This work develops sustainable Chitosan–CMC/ZnO–MgO nanocomposite films incorporating ZnO and MgO NPs synthesized from plant extracts. The effects of MgO concentration on particle distribution, matrix–filler bonding, crystalline features, heat resistance, mechanical performance, electrical response, and surface wettability were examined. Crystal violet photodegradation and antimicrobial effectiveness were also evaluated. The resulting multifunctional films may offer an eco-friendly material system for pollutant removal, antimicrobial surface coatings, and biodegradable functional applications.

2. MATERIALS AND METHODS

Chitosan possessing an average molecular weight of 85,000–124,000 g mol^{-1} and a deacetylation degree of ≥95%, along with carboxymethyl cellulose (CMC) exhibiting a viscosity of 400–800 cP for a 2 wt.% solution at 20 °C, was procured from Star Scientific Enterprises, Erode, Tamil Nadu, India. Magnesium nitrate hexahydrate and zinc acetate dihydrate acquired from the same manufacturer were employed as precursor salts for producing MgO NPs and ZnO NPs, respectively. All reagents were of analytical grade and used without further purification. Deionized water served as the solvent during polymer-solution formulation, botanical-extract processing, and nanoparticle-suspension preparation. Fresh okra and guava leaves collected from natural sources were used to prepare the plant-mediated extracts required for nanoparticle synthesis.

2.1 Preparation of Plant Extracts

Aqueous extracts from okra and guava leaves were employed as bioactive reaction-mediating and stabilizing agents during nanoparticle formation. To prepare the okra-leaf extract, 10 g of dried okra leaves were rinsed with Deionized Water (DIW), combined with 100 mL of DIW, and agitated at 50 °C for 3 h. Plant debris were separated by centrifugation, after which 40 mL of clarified supernatant was recovered for MgO nanoparticle synthesis.

For guava-leaf extract, 10 g of dried powdered leaves were dispersed in 100 mL of DIW and stirred at 700 rpm and 60 °C for 2 h. The dispersion was then ultrasonicated at 40 kHz and 60 °C for another 2 h, and then stored overnight in the dark at room temperature. Remaining solids were eliminated by filtration and centrifugation, and the recovered liquid fraction was utilized for ZnO NP synthesis.

2.2 Plant-mediated Synthesis of MgO and ZnO NPs

Guava and okra leaf extracts were used individually to prepare ZnO and MgO NPs because variations in their phytochemical profiles may influence precursor complexation, nucleation, particle growth, and stabilization differently. Using separate botanical sources does not mean either extract is inherently incapable of producing the alternative metal oxide. Guava leaf extract was selected for ZnO NP formation because its phenolic and flavonoid compounds can complex Zn^{2+} ions, regulate $Zn(OH)_2$ formation, and stabilize the ZnO particles produced after thermal conversion. Okra leaf extract was selected for MgO NP preparation because its phytochemicals and polysaccharides can coordinate Mg^{2+} ions, support precursor hydrolysis or precipitation, and restrict particle agglomeration. This plant-assisted strategy was adopted to produce stable nanoparticles with appropriate physicochemical features for incorporation into the Chitosan–CMC matrix. Fig. 1 illustrates the plant-mediated synthesis routes for MgO and ZnO NPs. The schematic summarizes precursor preparation, hydrothermal processing, separation, and drying.

Fig. 1: Plant-mediated synthesis of MgO and ZnO NPs

2.3 Okra-mediated Hydrothermal Preparation of MgO NPs

MgO NPs were fabricated through an okra-leaf-extract-mediated hydrothermal process (Ebenezer *et al.* 2026). The metal precursor mixture was formulated by diluting 5 mL of magnesium nitrate hexahydrate solution with 35 mL of DIW. The mixture was introduced gradually into 40 mL of okra leaf extract with simultaneous agitation and ultrasonication. Following continuous mixing at ambient temperature for 3 h, the resulting suspension was loaded into a Teflon-lined stainless-steel autoclave and heated at 100 °C for 12 h (Losetty *et al.* 2024). The precipitate was isolated by centrifugation, washed several times with distilled water to remove residual ions and organic compounds, and dried for 1 day. The dried material was calcined in a PLF110/10 furnace at 500 °C for 3 h with a controlled heating rate of 3 °C min^{-1} to enhance its crystalline structure.

2.4 Guava-leaf-mediated Hydrothermal Production of ZnO NPs

ZnO NPs were prepared hydrothermally using guava leaf extract as a complexing and stabilizing medium (Mathew *et al.* 2026). Initially, 40 mL of botanical extract was combined with 40 mL of 0.20 M zinc acetate dihydrate solution, formulated by dissolving 1.76 g of zinc acetate dihydrate in 40 mL of deionized water. The resulting dispersion was agitated at 700 rpm and 60 °C for 2 h and sonicated in a water bath at 30 °C for 1 h. Thereafter, mixing was continued at 700 rpm and 60 °C for another 2 h. The reaction medium was then placed in Teflon vessels and subjected to hydrothermal processing at 120 °C for 12 h. Finally, the generated ZnO NP suspension underwent additional ultrasonication and vacuum-oven drying. The recovered powder was preserved for physicochemical characterization and nanocomposite-film fabrication.

2.5 Fabrication of Chitosan–CMC/ZnO–MgO Composite Films

Chitosan–CMC/ZnO–MgO films were fabricated through solution casting followed by hydrothermal treatment. The polymer blend contained 0.70 g chitosan and 0.30 g CMC, giving a chitosan:CMC mass ratio of 70:30. Initially, 0.70 g chitosan was slowly added to 40 mL of 1% (v/v) aqueous acetic acid and mixed continuously until fully dissolved (Thungphotrakul and Prapainainar, 2024). After the solution reached room temperature, 0.30 g of CMC was added, and agitation was continued for 3 h to obtain a uniform chitosan–CMC solution. Each formulation included green-synthesized ZnO NPs at 30 mg, equivalent to 3 wt.% of the 1.00 g total polymer content. MgO NPs were subsequently incorporated at different concentrations based on the combined polymer mass. As presented in Table 1, the samples were identified as Chitosan–CMC/ZnO, 1% MgO, 2% MgO, and 3% MgO. Before blending, the specified quantities of ZnO and MgO NPs were suspended in 10 mL of distilled water by ultrasonication to reduce particle aggregation. The suspension was added to the polymer mixture and sonicated again to promote uniform distribution. Finally, the composite dispersion was agitated at room temperature for 24 h before hydrothermal processing.

Table 1. Composition of Chitosan–CMC/ZnO–MgO nanocomposite films and nanoparticle loading ratios

Sample	Chitosan:CMC Ratio	ZnO Content (wt.%)	MgO Content (wt.%)
Chitosan–CMC/ZnO	70:30	3	0
1% MgO	70:30	3	1
2% MgO	70:30	3	2
3% MgO	70:30	3	3

2.6 Hydrothermal Processing and Casting of Nanocomposite Films

After nanoparticle addition, the uniform Chitosan–CMC/ZnO–MgO dispersions underwent hydrothermal processing to facilitate interfacial interactions between the polymer chains and inorganic particles. Each prepared dispersion was placed in a sealed Teflon-lined stainless-steel autoclave and maintained at 120 °C for 12 h. After the vessels cooled naturally to ambient temperature, 70 mL of each treated formulation was transferred into glass Petri dishes with level bases. The mixtures spread freely across the dishes without employing a film-casting applicator. Solvent removal was performed in an oven at 70 °C for 1 day, producing continuous nanocomposite films. Before mechanical characterization, the thickness of each obtained film was determined to be 0.20 ± 0.01 mm.

2.7 Mechanical Performance

Film strength and extensibility were quantified using a ZwickRoell Z010 universal testing system equipped with a 10 kN load cell, in accordance with ISO 527-3 (Mohammadi *et al.* 2024). Specimens measuring 0.20 ± 0.01 mm in thickness were stretched at a crosshead velocity of 200 mm/min, and their tensile strength and elongation were recorded. Shore A hardness was determined with a Bareiss DigiTest durometer in accordance with ISO 7619-1.

2.8 Thermal Characterization and Kissinger Kinetic Evaluation

Thermal performance was examined by thermogravimetric analysis (TGA) using a Shimadzu

TG-60 system under nitrogen from 25 to 600 °C. The primary TGA measurement was conducted at 20 °C min^{-1}, while additional runs at 5, 10, and 15 °C min^{-1} were performed for kinetic analysis. Differential scanning calorimetry (DSC) was performed using a Shimadzu DSC-60 under a nitrogen atmosphere from 25 to 250 °C at a heating rate of 10 °C min^{-1}.

The apparent activation energy, E_a associated with thermal decomposition was determined using the Kissinger procedure. The maximum degradation temperature (T_p) was extracted from the derivative thermogravimetry (DTG) peaks recorded at heating rates of 5, 10, 15, and 20 °C min^{-1}. Kissinger relationship was expressed as follows (Vaikundam *et al.* 2026):

$$\ln\left(\frac{\beta}{T_p^2}\right) = -\frac{E_a}{RT_p} + C \quad \ldots (1)$$

Here, β denotes the programmed heating rate in K min^{-1}, and T_p represents the absolute temperature in K corresponding to the maximum DTG degradation rate. E_a is the apparent decomposition activation energy, while R is 8.314 J mol^{-1} K^{-1} when E_a were expressed in J mol^{-1}. C represents the intercept associated with kinetic and reaction-dependent factors.

For each formulation, $\ln\left(\beta/T_p^2\right)$ was plotted against $1/T_p$. Linear regression produced a slope equal to - E_a/R from which E_a was calculated. Larger E_a values for the ZnO$^-$ and MgO$^-$containing films suggested a higher energetic barrier to degradation, potentially resulting from reduced polymer-chain mobility and stronger matrix-nanoparticle interactions. Films exposed to hydrothermal processing also exhibited higher E_a values, indicating improved resistance to thermal decomposition.

2.9 Wettability and Surface Free-energy Determination

Film wettability was characterized at room temperature with a Fytronix 9000 goniometer following ASTM D7490-13. DIW served as the polar testing liquid, whereas diiodomethane (DIM), which has predominantly dispersive behavior, was selected as the nonpolar liquid. For both liquids, static contact angles were recorded at no fewer than 3 separate positions on each specimen. Mean contact-angle values were subsequently applied to calculate surface free energy.

Total surface free energy and its polar and dispersive contributions were estimated through the Owens-Wendt-Kaelble model:

$$\gamma_s = \gamma_s^d + \gamma_s^p \quad \ldots (2)$$

The interfacial relationship for each probe liquid was expressed as:

$$\gamma_l(1+\cos\theta) = 2\left[\left(\gamma_s^d\gamma_l^d\right)^{\frac{1}{2}} + \left(\gamma_s^p\gamma_l^p\right)^{\frac{1}{2}}\right] \ldots (3)$$

Here, θ is the measured contact angle in degrees; γ_l represents the probe-liquid surface tension in mNm^{-1}; and γ_l^d and γ_l^p correspond to its dispersive and polar contributions, respectively. Similarly, γ_s^d and γ_s^p denote polar and dispersive components of solid surface free energy, and γ_s indicates their combined value.

2.10 Frequency-dependent Dielectric Response

Electrical behavior was examined from 1 kHz to 1 MHz with a Fytronix 9000 Analyzer. Specimens were compressed under 5 tons into circular pellets 0.05 cm thick and 13 mm in diameter. Increasing frequency produced lower dielectric-constant values but higher AC conductivity. This frequency dependence was attributed to Maxwell–Wagner–Sillars interfacial polarization. Nanoparticle incorporation increased the low-frequency dielectric constant because mobile charges accumulated at interfaces between the polymer matrix and inorganic phases. The simultaneous presence of ZnO and MgO improved the dielectric response through increased interfacial polarization.

2.11 Agar-diffusion Assessment of Antimicrobial Activity

Antimicrobial performance was assessed using the agar-diffusion technique with Gram-positive *S. aureus*, the yeast *C. albicans*, and the Gram-negative *E. coli*. Bacterial cultures were prepared on Mueller–Hinton agar, whereas yeast cultures were prepared on Sabouraud dextrose agar. Each microbial suspension was adjusted to 10^6–10^7 CFU mL^{-1} and distributed uniformly across sterile agar plates. Film specimens were positioned on the inoculated surfaces and maintained at 37 °C for 1 day. After incubation, inhibition-zone diameters surrounding the specimens were recorded in mm.

2.12 Photocatalytic Activity

Photocatalytic performance of Chitosan–CMC/ZnO–MgO films was investigated by degrading crystal violet (CV) under ultraviolet A (UVA) exposure. Experiments were conducted in a 150 mL Pyrex reactor illuminated by 2–8 W fluorescent lamps with peak emission at 365 nm. A constant lamp-to-liquid distance of 8.5 cm was maintained. Irradiance was recorded using a Delta OHM DO9721 radiometer.

The 150 mg of film was immersed in 50 mL of 20 mg L^{-1} CV solution. The suspension was stirred and exposed to UVA radiation for 140 min. Samples withdrawn at predetermined intervals were centrifuged, and supernatant absorbance was measured at approximately 590 nm with a Shimadzu UV-1800

spectrophotometer. Degradation efficiency was determined using:

$$\text{Degradation efficiency (\%)} = \frac{C_0 - C_t}{C_0} \times 100 \quad \ldots (4)$$

Pseudo-first-order kinetics were evaluated using:

$$\ln\left(\frac{C_0}{C_t}\right) = kt \quad \ldots (5)$$

Here, C_0 and C_t denote the CV concentrations after dark equilibration and at irradiation time t, respectively; t were expressed in min; and k represents apparent pseudo-first-order constant in min^{-1}. Value of k was obtained from the slope of $\ln(C_0/C_t)$ against t. Photoexcitation of ZnO and MgO generated electron-hole pairs, which promoted ROS formation and subsequent CV degradation.

2.13 Characterization

The physicochemical characteristics of chitosan–TiO_2 nanocomposite films were evaluated through complementary spectroscopic, microscopic, and diffraction methods. Functional groups and possible molecular interactions within film samples were identified by a Thermo Scientific Fourier-transform spectrometer. Spectra were collected using the KBr disc technique across 400–4000 cm^{-1} with a spectral resolution of 4 cm^{-1} (Kashyap *et al.* 2026).

Film-surface morphology and elemental distribution were examined using a Zeiss Gemini SEM coupled with an energy-dispersive X-ray detector. Before microscopic observation, the dried films were sectioned into specimens measuring approximately 5 × 5 mm. Each specimen was fixed onto an aluminum stub with carbon tape and coated with a thin gold film by sputtering to prevent charge accumulation during electron-beam exposure. The prepared specimens were subsequently examined under the selected SEM operating conditions.

The crystalline characteristics and phase composition of the films were determined using a Bruker D8 Advance X-ray diffractometer. Measurements were conducted with Cu Kα radiation. Diffraction profiles were acquired over the angular interval of $10° \leq 2\theta \leq 80°$.

2.14 Statistical Evaluation of Experimental Data

The pure chitosan and chitosan–TiO_2 nanocomposite films containing 5, 10, and 20 mL of TiO_2 nanoparticle suspension were prepared in triplicate (n = 3). Results are reported as mean ± standard deviation. Differences among the film formulations were examined using one-way analysis of variance (ANOVA). Statistical significance was accepted at $p < 0.05$. Data analysis was performed using the selected statistical software, and the reproducibility of the experimental findings was assessed from the variation among replicate measurements.

3. RESULTS AND DISCUSSION

3.1 Physicochemical Assessment of MgO NPs

The surface configuration, elemental composition, and crystalline characteristics of the synthesized MgO NPs were examined through SEM, EDX, and XRD measurements. The SEM micrograph in Fig. 2(a) shows densely clustered particles with irregular, approximately spherical features. This aggregation may be attributed to attractive interactions among nanosized particles possessing high surface energy during the hydrothermal preparation process.

The EDX spectrum in Fig. 2(b) confirms the presence of Mg and O, with measured elemental proportions of Mg (54.10%) and O (45.90%). These findings support the successful production of MgO NPs. Furthermore, the absence of detectable impurity-related peaks suggests that the prepared material possesses high elemental purity.

As illustrated in Fig. 2(c), the diffraction profile contains reflections corresponding to the cubic periclase phase of MgO. The prominent reflection detected at approximately 42.9°, indexed to the (200) crystallographic plane, verifies the formation of crystalline MgO. The remaining diffraction peaks also match the standard pattern of cubic MgO, confirming successful formation of the intended crystalline structure.

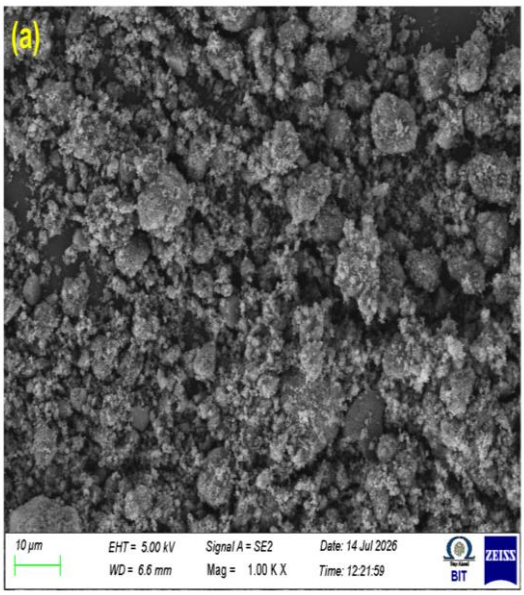

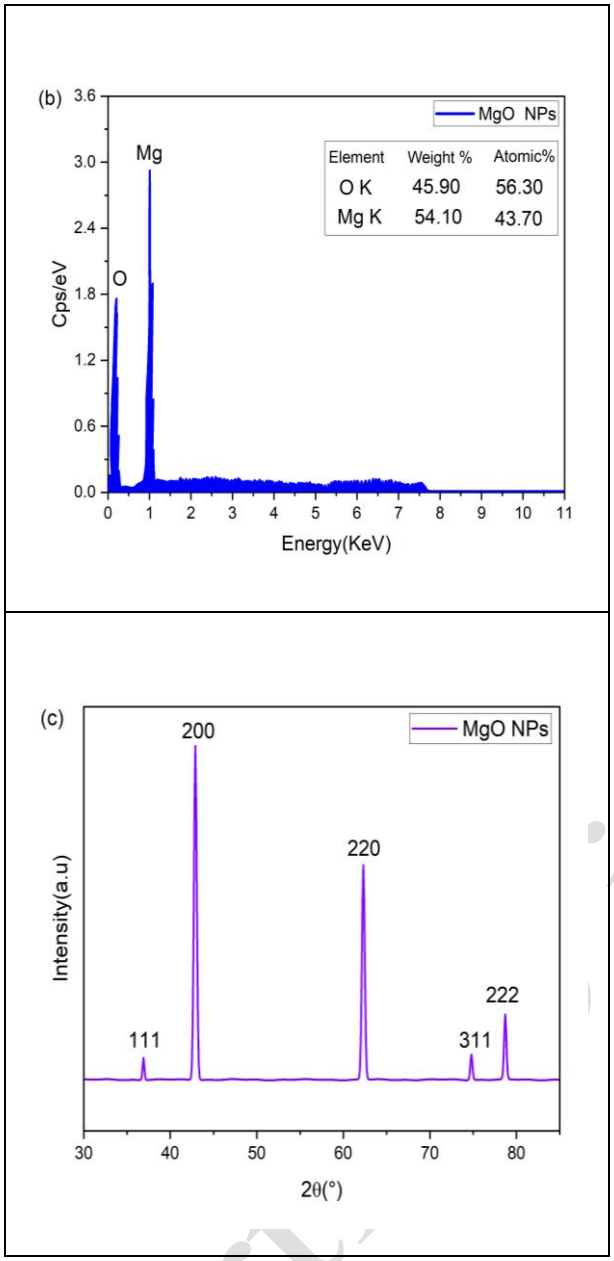

Fig. 2: Characterization of the synthesized MgO NPs: (a) SEM micrograph, (b) EDX spectrum, and (c) XRD pattern

3.2 Morphological, Elemental and Crystallographic Evaluation of ZnO NPs

The morphology, elemental composition, and crystallinity of ZnO NPs were assessed through SEM–EDX and XRD. Fig. 3(a) displays compact particle clusters with an uneven granular texture. This aggregation is associated with elevated nanoparticle surface energy and interparticle attraction during biogenic preparation. The EDX spectrum (Fig. 3(b)) identifies Zn and O as the major elements, verifying ZnO formation. A weak carbon signal may originate from plant-derived surface residues or conductive carbon tape. Oxygen represents the ZnO lattice and does not independently confirm organic capping.

The XRD diffractogram (Fig. 3(c)) verifies hexagonal wurtzite ZnO rather than metallic Zn (Zn^0). Reflections at approximately 2θ = 31.8°, 34.4°, 36.3°, 47.5°, 56.6°, 62.9°, 67.9°, and 69.3° were assigned to the (100), (002), (101), (102), (110), (103), (112), and (201) planes, respectively. These reflections agree well with the standard JCPDS card No. 36-1451, confirming the hexagonal wurtzite structure of ZnO. The 38.20° (111) reflection is not characteristic of wurtzite ZnO and may indicate an impurity or substrate contribution. The intense (101) reflection indicates good crystallinity of the synthesized ZnO NPs. The diffraction pattern obtained in this study is consistent with previous reports on green-synthesized ZnO NPs. ZnO NPs synthesized using *Rubus fairholmianus* root extract exhibited an XRD pattern matching the same JCPDS card (36-1451), with an average crystallite size of 11.34 nm calculated using the Debye–Scherrer equation (Rajendran *et al.* 2021).

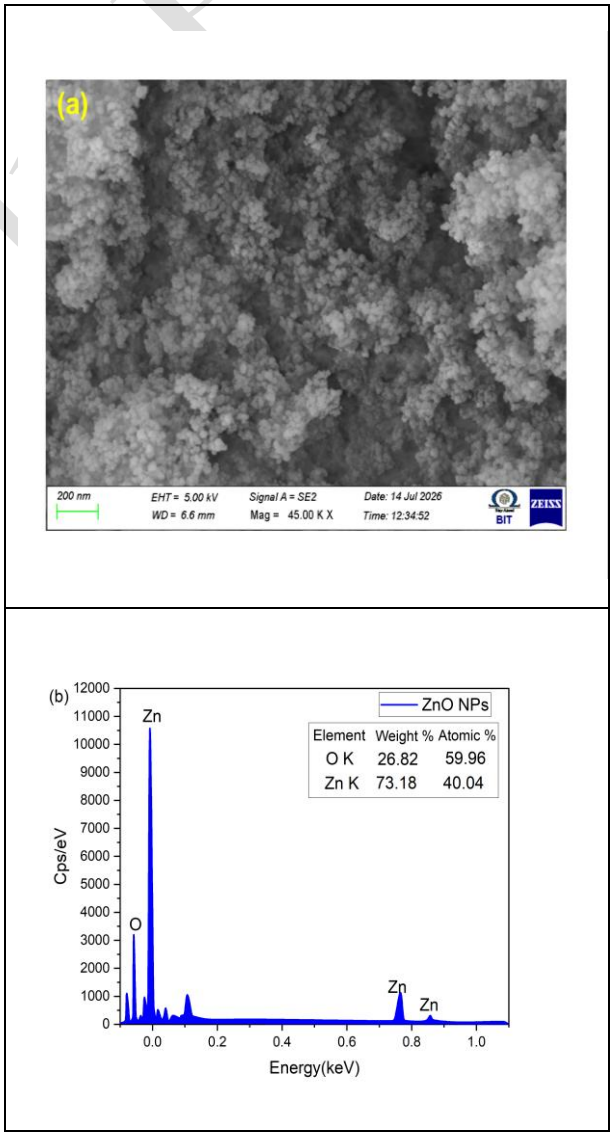

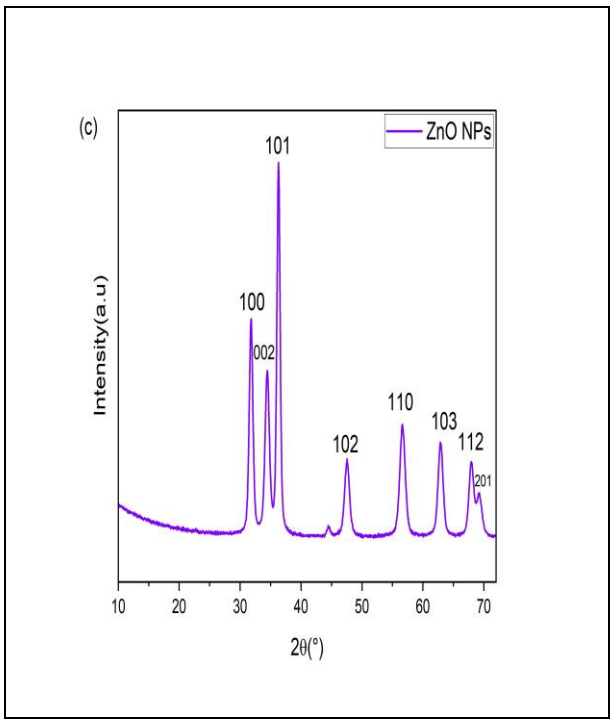

Fig. 3: Morphological, elemental, and crystallographic characterization of ZnO NPs: (a) SEM micrograph, (b) EDX spectrum, and (c) XRD profile

3.3 FT-IR Characterization of MgO and ZnO NPs

The FT-IR profiles of the biogenic MgO and ZnO NPs are presented in Fig. 4. Both spectra contain absorption bands associated with surface functional groups and metal–oxygen vibrations. For MgO NPs, the broad signal centered at 3462 cm^{-1} corresponds to O–H stretching from surface hydroxyl groups and adsorbed moisture. The weak features at 2348 and 1992 cm^{-1} may arise from atmospheric CO_2 and combination or overtone vibrations, respectively. The absorption at 1592 cm^{-1} is associated with H–O–H bending, whereas the 1386 cm^{-1} band may originate from nitrate or carboxylate vibrations associated with residual phytochemicals. The intense band near 470 cm^{-1} is assigned to Mg–O stretching and confirms MgO formation.

For ZnO NPs, the broad absorption at 3428 cm^{-1} is attributed to hydroxyl stretching. Signals at 2924 and 2856 cm^{-1} represent symmetric and asymmetric stretching of C–H bonds, respectively. The 1632 cm^{-1} band may correspond to adsorbed water bending or carbonyl-containing surface compounds. The feature near 1028 cm^{-1} is attributed to C–O or C–O–C from plant-derived biomolecules retained on the nanoparticle surface. These compounds may function as complexing and stabilizing agents rather than directly reducing Zn^{2+} to metallic Zn^0 during ZnO formation. Zn–O vibrations are expected in the low-wavenumber region and provide direct evidence of the ZnO lattice.

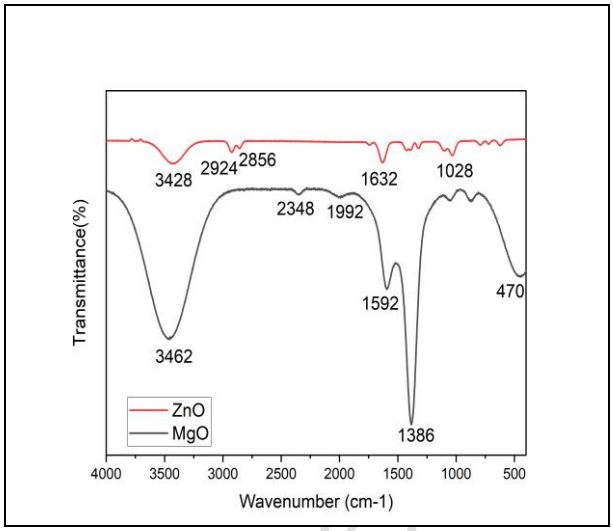

Fig. 4: FT-IR spectra of biogenic MgO/ZnO NPs

3.4 FT-IR Analysis

Fig. 5 shows FT-IR profiles of Chitosan–CMC/ZnO–MgO nanocomposite films, revealing interactions between the biopolymer network and incorporated metal-oxide nanoparticles. All formulations displayed a broad absorption envelope between 3420 and 3472 cm^{-1}, assigned to overlapping O–H and N–H stretching vibrations from CMC and chitosan, respectively. The band position shifted from 3420 cm^{-1} in the Chitosan–CMC/ZnO film to 3472 cm^{-1} following MgO incorporation. This spectral displacement indicates that MgO altered the local hydrogen-bonding environment and interactions among chitosan, CMC, ZnO, and MgO. However, a shift to a higher wavenumber alone does not necessarily demonstrate stronger intermolecular hydrogen bonding.

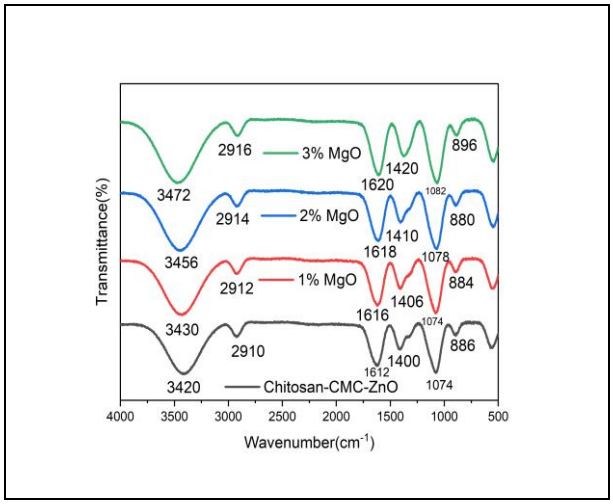

Fig. 5: FT-IR spectra of the Chitosan–CMC/ZnO–MgO nanocomposite films

Absorptions between 2910 and 2916 cm^{-1} correspond to aliphatic C–H stretching. Their occurrence in every formulation indicates that nanoparticle loading did not substantially alter the main polysaccharide framework. The signals recorded at 1612–1620 cm^{-1} can be assigned to overlapping H–O–H bending, chitosan amide vibrations, and asymmetric COO^- stretching from CMC. Features within 1400–1420 cm^{-1} originate primarily from symmetric COO^- stretching and C–H deformation. Variations in their position or intensity with increasing MgO content suggest changes in interactions between the metal oxides and polymer functional groups.

The 1074–1082 cm^{-1} region represents C–O and C–O–C within polysaccharide chains. Minor shifts in these bands support interfacial interactions among chitosan, CMC, ZnO, and MgO. Increased band intensity alone cannot confirm stronger interactions because it can also depend on sample thickness and concentration. Signals appearing at 880–896 cm^{-1} are associated with saccharide-ring or glycosidic-linkage vibrations. The absorptions between 500 and 600 cm^{-1} are attributed to overlapping metal–oxygen lattice vibrations, supporting the incorporation of ZnO and MgO into the Chitosan–CMC matrix. This result agrees with green-synthesized MgO NPs reported in previous studies, using *Camellia sinensis* extract, where a stretching band at 470.63 cm^{-1} similarly confirmed MgO lattice formation, alongside a broad O–H absorption from surface hydroxyl groups (Ghanbari *et al.* 2023).

3.5 SEM–EDX Examination

Surface characteristics and elemental composition of the Chitosan–CMC/ZnO reference film were evaluated using SEM coupled with EDX. The SEM micrograph (Fig. 6) revealed a comparatively homogeneous, fine-textured surface containing limited microscale irregularities. The absence of prominent particle clusters suggests that ZnO was reasonably distributed throughout the biopolymer matrix.

EDX measurements identified carbon (C, 39.45 wt.%) and oxygen (O, 38.11 wt.%) as the principal elements, mainly originating from the Chitosan–CMC network and ZnO. Detection of nitrogen (N, 6.42 wt.%) supports the presence of chitosan, whereas zinc (Zn, 10.87 wt.%) verifies the incorporation of Zn-containing nanoparticles. However, EDX identifies elements rather than their oxidation states; therefore, it cannot independently confirm that Zn occurs specifically as ZnO. Minor silicon (Si, 3.25 wt.%) and aluminum (Al, 1.12 wt.%) signals may arise from the sample substrate, mounting materials, preparation procedure, or trace contamination.

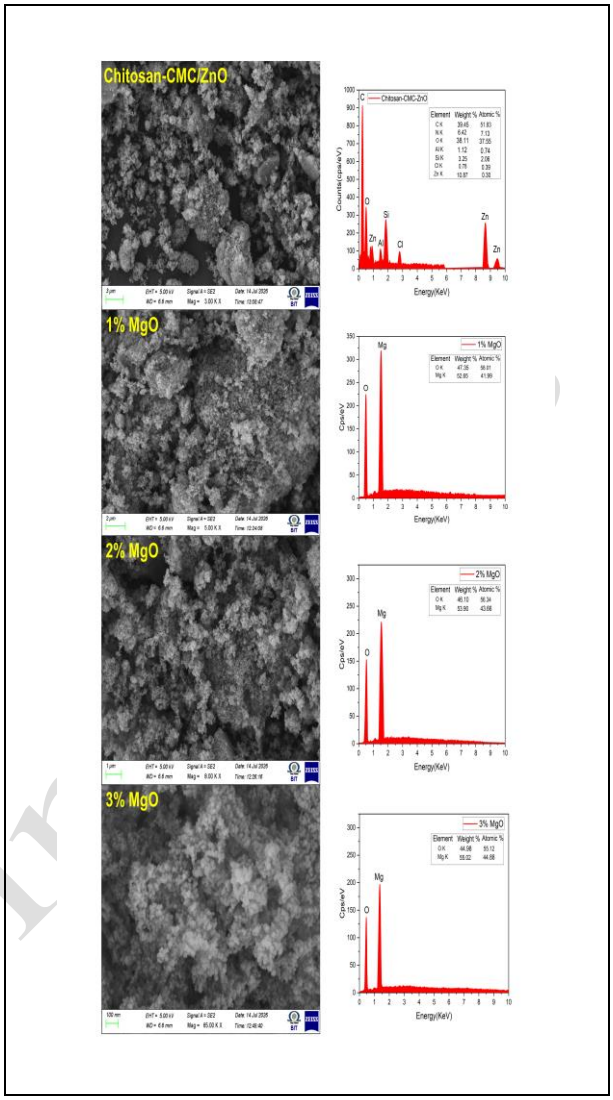

Fig. 6: SEM micrographs and EDX spectra of the nanocomposite films

Introducing 1 wt.% MgO produced a compact and comparatively even film surface, indicating effective nanoparticle distribution within the Chitosan–CMC/ZnO matrix. No prominent MgO clusters were evident at this concentration. The corresponding EDX results contained Mg (52.65 wt.%) and O (47.35 wt.%), supporting MgO formation. However, an EDX spectrum containing only Mg and O is representative of isolated MgO NPs rather than the complete nanocomposite film, which should also contain C, N, Zn, and other matrix-related elements. The absence of additional signals indicates no detectable impurities within the selected MgO-rich region.

At 2 wt.% MgO, particle-enriched regions became more apparent, although the additive remained reasonably distributed across the film. EDX recorded Mg and O contents of 53.90 wt.% and 46.10 wt.% with corresponding atomic percentages of 43.66% and 56.34%. These findings support the presence of compositionally pure MgO in the examined region. The

small difference in Mg content relative to the 1 wt.% formulation cannot independently confirm increased MgO loading because EDX is a localized, semiquantitative technique. Nevertheless, no additional elements attributable to detectable contamination were observed. These morphological and elemental observations align with previous chitosan-ZnO nanocomposite films. A green-synthesized ZnO/chitosan film similarly showed a smooth, compact surface with minor ZnO aggregates, and an EDX profile dominated by C, O, Zn, and N, confirming chitosan as an effective substrate for ZnO dispersion (Alamdari *et al.* 2022)

Increasing MgO concentration to 3 wt.% produced a rougher, less homogeneous surface with localized particle clusters, indicating reduced dispersion efficiency at higher loading. The MgO-rich area exhibited Mg (55.02 wt.%; 44.88 at%) and O (44.98 wt.%; 55.12 at%), without detectable impurity signals. Tensile strength and hardness improved throughout the investigated concentration range, indicating that the reinforcing contribution of MgO remained greater than the adverse influence of aggregation under the applied conditions. However, the morphology of the 3 wt.% film suggests that the dispersion threshold was being approached. Further MgO addition could promote larger agglomerates, compositional heterogeneity, and stress-concentration regions, potentially reducing functional and mechanical performance of nanocomposite films.

3.6 XRD Analysis

The diffraction profiles of Chitosan–CMC/ZnO–MgO nanocomposite films were presented in Fig. 7. The Chitosan–CMC/ZnO reference film displayed a broad halo at approximately $2\theta \approx 19–20°$, reflecting the combined semi-crystalline and amorphous nature of the Chitosan–CMC matrix. This broad feature represents polymer-chain ordering rather than a specific crystallographic plane. All formulations exhibited a distinct reflection near 36.3°, indexed to the (101) plane of hexagonal wurtzite ZnO, consistent with JCPDS No. 36-1451. Its retention indicates that crystalline ZnO remained structurally stable after MgO incorporation.

At 2% and 3% MgO loading, the MgO-related reflections became increasingly distinguishable. The higher-angle peaks assigned to the (200), (220), (311), and (222) planes verify the presence of the cubic periclase MgO phase and agree with JCPDS No. 45-0946. These signals were weak at 1% MgO but intensified at 2% and especially at 3%, indicating a greater contribution from crystalline MgO. The reflection at 36.3° belongs to ZnO and should not be interpreted as evidence of increasing MgO content. The polymer halo persisted in every formulation but showed reduced intensity following MgO addition. This variation suggests disturbed polymer-chain organization; however, intensity reduction may also result from matrix dilution and should not be taken alone as proof of decreased crystallinity.

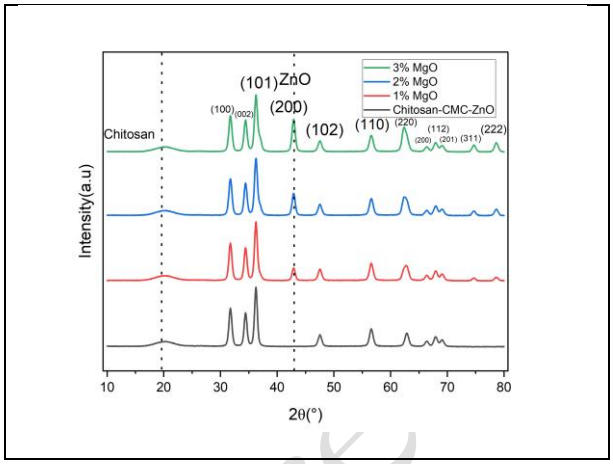

Fig. 7: XRD patterns of the nanocomposites

3.7 Mechanical Performance

Fig. 8 compares tensile strength (TS) and Shore A hardness of Chitosan–CMC/ZnO–MgO films. The Chitosan–CMC/ZnO reference sample recorded a tensile strength of 28.6 MPa. Adding 1, 2, and 3 wt.% MgO progressively raised the measured strength to 35.9, 43.8, and 51.6 MPa, respectively. Hardness followed the same pattern, increasing from 41.8 Shore A for the reference formulation to 47.6, 54.9, and 62.7 Shore A at corresponding MgO concentrations of 1, 2, and 3 wt.%.

This improvement may result from interfacial interactions between MgO and the Chitosan–CMC/ZnO network, which restrict polymer-chain movement and suppress slippage at deformation. Consequently, the films show greater resistance to surface indentation and higher tensile stress. A previous chitosan-based nanocomposite containing 0.5% MgO achieved a maximum tensile strength of 98 MPa together with improved thermal and antimicrobial performance (Mohamad *et al.* 2023).

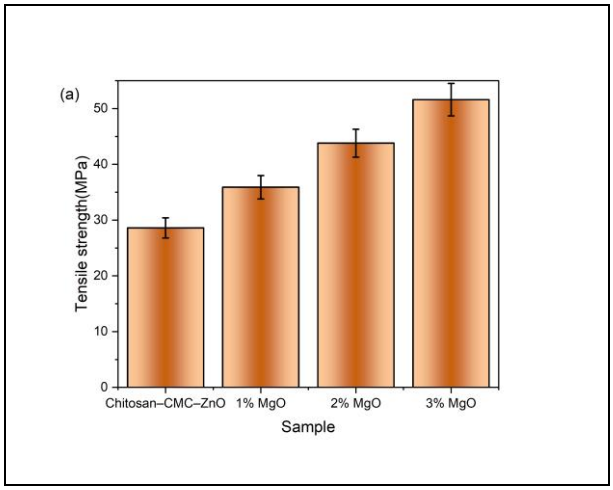

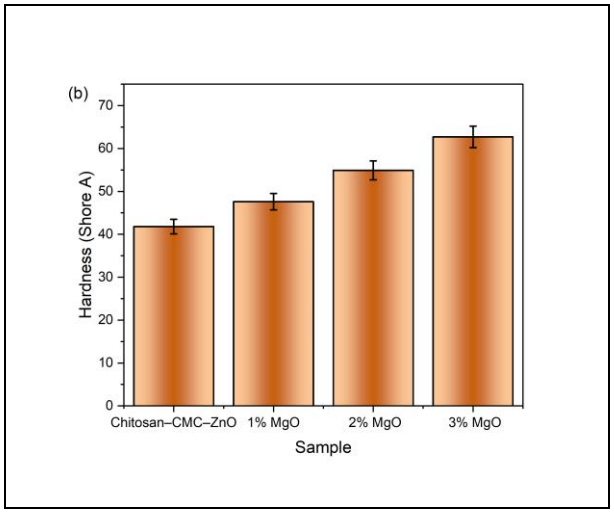

Fig. 8: (a) Tensile strength and (b) Shore A hardness of the nanocomposites

The simultaneous improvement in TS and Shore A hardness suggests that MgO NPs effectively reinforced the Chitosan–CMC/ZnO matrix. Across the examined concentration range, the inorganic particles likely promoted stress transmission through their interfacial contact with the polymer network. The FT-IR hydroxyl-stretching band shifted to a higher wavenumber, from 3420 to 3472 cm^{-1}, rather than to a lower wavenumber. This shift indicates a change in the hydrogen-bonding environment among Chitosan, CMC, ZnO, and MgO. Nevertheless, an upward shift alone cannot confirm stronger hydrogen bonding. Interfacial interactions can restrict chain movement and reduce molecular slippage, thereby improving resistance to tensile indentation and deformation.

Film containing 1 wt.% MgO NPs exhibited a dense and comparatively homogeneous surface, while particle-rich regions were evident at 2 and 3 wt.%. Although clustering was limited, hardness and strength continued to increase up to 3 wt.%, indicating that aggregation did not overcome the reinforcing effect within the tested range. However, the observed progressive improvement does not establish that concentrations above 3 wt.% would provide additional benefits. Greater loading could intensify agglomeration, generate stress-concentration regions, and compromise film integrity.

Collectively, MgO incorporation increased the measured surface hardness and tensile load-bearing ability of the Chitosan–CMC/ZnO films. Hardness represents resistance to indentation and should not independently be interpreted as rigidity or elastic stiffness. Since elastic modulus and elongation at break were not measured, the relationship among stiffness, strength, and ductility remains undetermined. Future investigations could include complete stress–strain measurements and cyclic loading tests to identify an appropriate MgO concentration for the intended film application.

3.8 Thermal Behaviour

Thermal performance strongly influences the suitability of polymer nanocomposites for processing and elevated-temperature applications. Improved heat resistance can delay decomposition and help preserve material integrity. However, greater thermal stability does not automatically improve processability, which also depends on viscosity, processing temperature, and film-forming behavior.

TGA and DSC were employed to evaluate the thermal characteristics of the Chitosan–CMC/ZnO–MgO films, as shown in Figs. 9(a–b). The TGA profiles exhibited generally comparable multistage mass-loss patterns. Nevertheless, MgO-containing formulations showed delayed degradation relative to the Chitosan–CMC/ZnO reference film, which should not be described as a pure sample because it already contains ZnO. This shift may result from MgO–polymer interfacial interactions that restrict chain movement and hinder the transport of volatile decomposition products.

The remaining mass at elevated temperatures also increased with MgO concentration because MgO is an inorganic, thermally persistent component. This higher residue confirms greater inorganic content within the films. Residual mass alone does not establish improved thermal stability; this conclusion should also be supported by increased onset, maximum degradation, or characteristic mass-loss temperatures. Collectively, delayed decomposition and increased residue suggest that MgO incorporation enhanced the thermal resistance of the Chitosan–CMC/ZnO matrix within the investigated range.

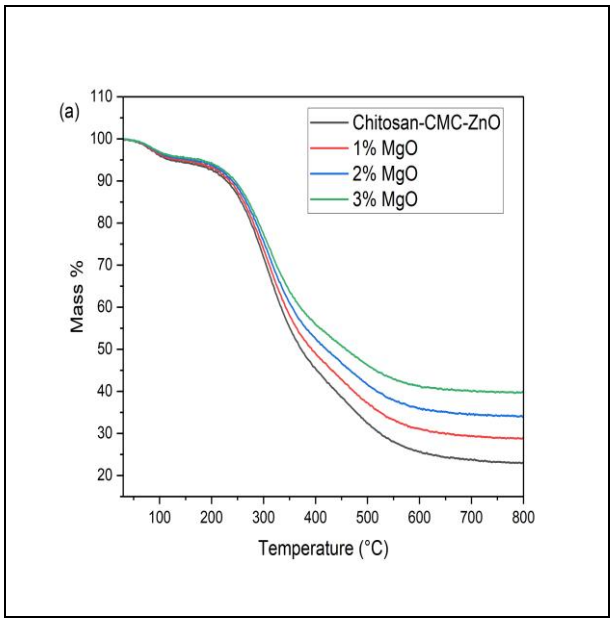

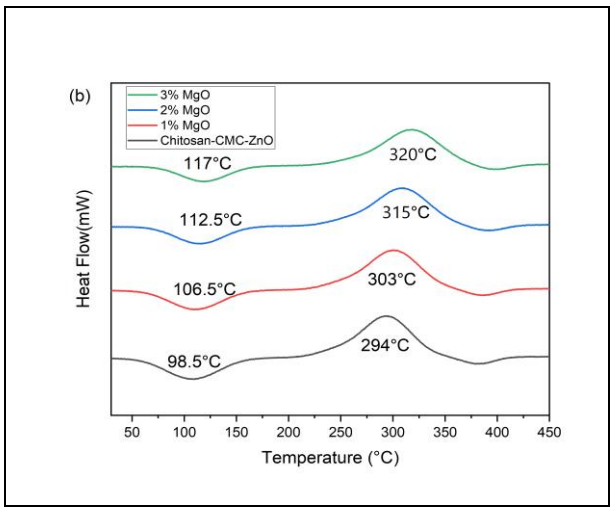

Fig. 9: TGA and DSC thermal profiles of the nanocomposite films

DSC measurements showed a glass-transition temperature (T_g) of approximately 98.5 °C for the Chitosan–CMC/ZnO reference film rather than a pure sample. Following MgO incorporation, T_g increased successively to 106.5 °C, 112 °C, and 117 °C. This upward trend suggests that MgO–polymer interfacial interactions constrained segmental chain motion, producing a less mobile matrix. Assigning these temperatures to T_g should be based on a DSC baseline shift rather than an endothermic peak.

A thermal event near 294 °C remained visible in every formulation. This high-temperature feature is more appropriately associated with polymer decomposition or a degradation-related transition, rather than confirming that the original matrix structure remained unchanged. Its persistence indicates that MgO addition did not markedly alter the principal high-temperature thermal event within the investigated concentration range.

Improved thermal resistance is valuable when nanocomposite films must retain their properties under elevated temperatures or changing environmental conditions. This behavior can support their potential use in packaging, coatings, and sensing systems, although application-specific performance requires further testing. A previous study reported that MgO incorporation into a different bio-based chitosan film increased crystallinity to 84.9% and thermal stability to 265 °C, while additional bioactive modification produced an elongation at break of 15.29% and antioxidant activity of 70.16% DPPH scavenging (Valsalan *et al.* 2026).

3.9 Thermal-decomposition Kinetics

The apparent activation energy (E_a) of thermal decomposition was estimated using the Kissinger approach. Linear plots were constructed between $\ln(\beta/T_p^2)$ and $1000/T_p$, where β represents the heating rate, and T_p denotes the maximum degradation temperature. The Kissinger calculation requires T_p values obtained at several heating rates; a single heating rate is insufficient to determine E_a.

As displayed in Fig. 10, every formulation produced a linear regression with R^2 = 0.9999. This strong correlation indicates good agreement with the Kissinger model, although a high R^2 alone does not establish complete kinetic reliability. The Chitosan–CMC/ZnO reference film exhibited an E_a of 86 kJ/mol. MgO incorporation increased E_a to 96, 108, and 122 kJ/mol for the 1%, 2%, and 3% MgO formulations, respectively.

The rising E_a values indicate that greater energy was required to initiate thermal decomposition after MgO addition. Interfacial interactions and restricted polymer-chain movement may hinder heat transfer and volatile-product diffusion within the matrix. Hydrogen bonding among the available functional groups may also contribute to this resistance. Overall, the results support improved thermal stability with increasing MgO content. However, "significant improvement" should be stated only when statistical testing confirms $p < 0.05$.

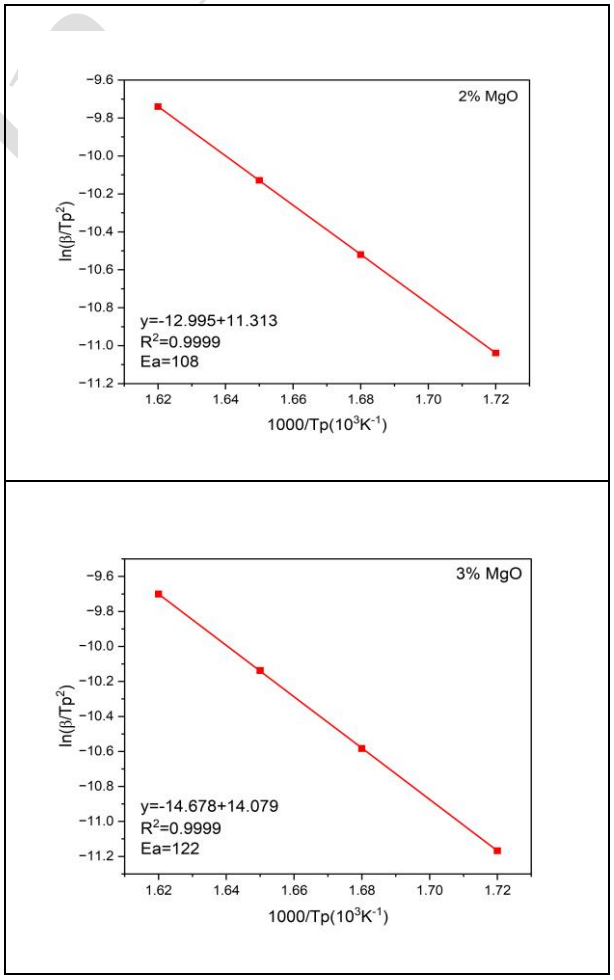

Fig. 10: Kissinger plots of the nanocomposite films containing 2% and 3% MgO

3.10 Wettability and Surface Free Energy

Surface wettability and free energy govern interfacial adhesion and interactions between nanocomposite films and their surrounding environment. These characteristics affect coating performance, biological interfaces, and surface physicochemical behavior. Therefore, contact-angle measurements were performed using water and diiodomethane, as shown in Fig. 11.

The Chitosan–CMC/ZnO reference film, rather than a pure sample, exhibited a water contact angle of 71.26°, indicating hydrophilic behavior. Increasing MgO content raised this value to 93.16° for the 3% formulation, indicating a transition to a comparatively hydrophobic surface. Diiodomethane contact angles changed only slightly among the formulations. However, limited variation in the diiodomethane angle alone cannot confirm that the dispersive surface-energy component remained constant; this component must be calculated using an established model such as Owens–Wendt.

A separate nanocomposite investigation reported that increasing Fe_2O_3 content increased the surface free energy from 41.36 to 66.23 mJ/m², accompanied by a reduction in water contact angle from 58.36° to 39.25° and improved dielectric behavior over 40 Hz–5.6 MHz (Abdeltwab *et al.* 2024).

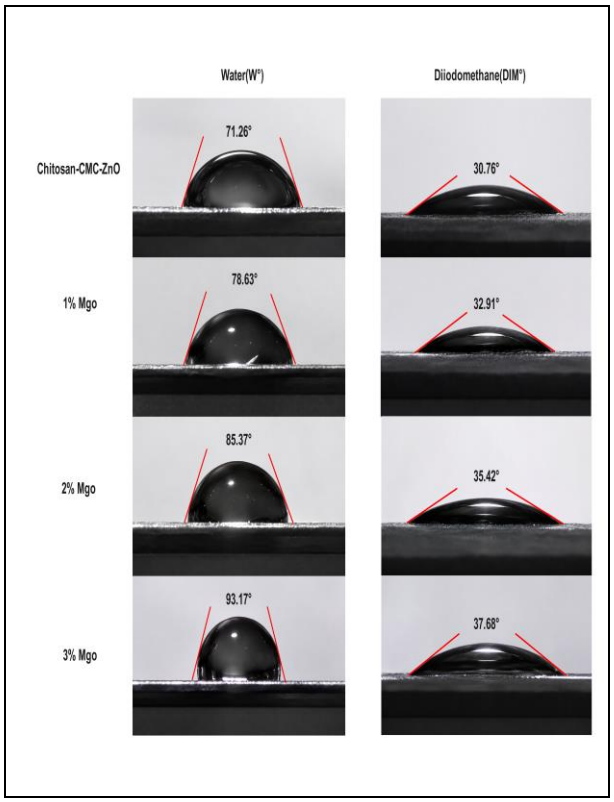

Fig. 11: Film–liquid contact angles of the nanocomposite films

3.11 Dielectric Behaviour

Dielectric characteristics describe how composite films respond to an alternating electric field and provide information about polarization and electrical-energy dissipation. The dielectric constant represents the material's polarization and charge-storage response, whereas dielectric loss quantifies dissipated electrical energy rather than directly indicating electrical stability.

Frequency-dependent dielectric measurements of the Chitosan–CMC/ZnO–MgO films are displayed in Fig. 12(a) and (b). As shown in Fig. 12(a), the dielectric constant (ε′) declined with increasing frequency for every formulation. The elevated ε′ values observed at low frequencies can be associated with dipolar orientation and interfacial polarization arising from the heterogeneous polymer–nanoparticle interfaces. Electrode polarization and mobile-charge accumulation may also contribute in this frequency region and should not automatically be attributed only to the Maxwell–Wagner–Sillars mechanism. At higher frequencies, slowly responding dipoles and interfacial charges cannot align completely with the rapidly alternating field. Consequently, their reduced contribution lowers the dielectric constant.

MgO incorporation increased the dielectric constant of the Chitosan–CMC/ZnO–MgO films relative to the Chitosan–CMC/ZnO reference formulation. The ε′ values increased progressively at MgO concentrations of 1%, 2%, and 3%, with the 3% formulation showing the highest response. This behavior may result from additional polymer–nanoparticle interfaces that facilitate charge accumulation and interfacial polarization.

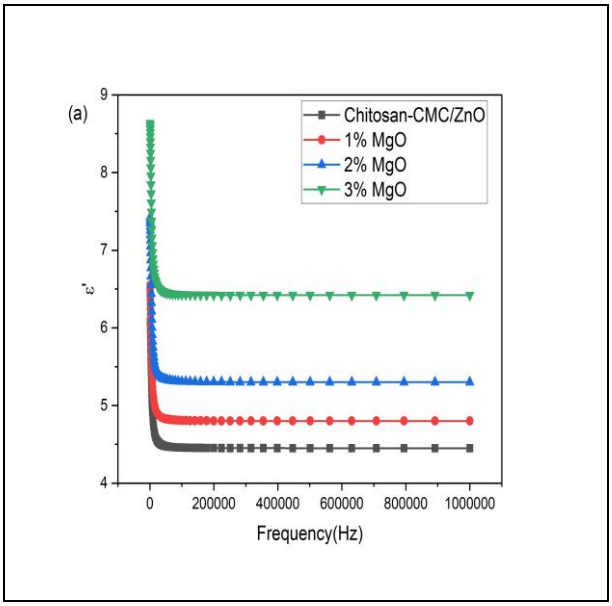

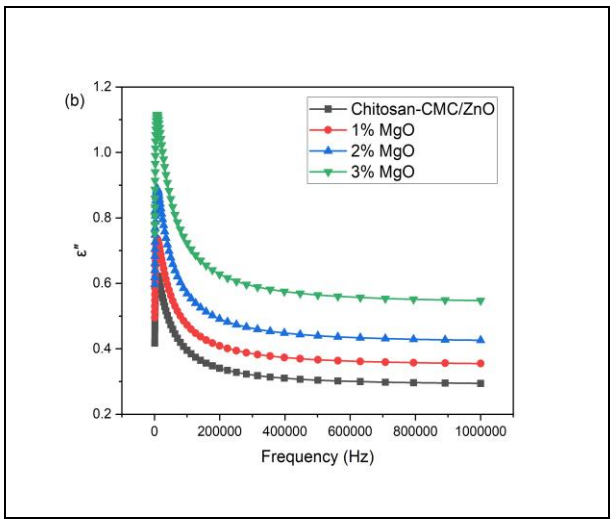

Fig. 12: Frequency-dependent dielectric response of the Chitosan–CMC/ZnO–MgO films: (a) dielectric constant (ε′) and (b) dielectric loss factor (ε″)

The increase in ε′ with increasing MgO concentration should not be attributed solely to an intrinsically high dielectric constant of MgO without comparing its permittivity with that of the polymer matrix. Previous research similarly indicates that dielectric response may peak at an optimum filler concentration because of favorable dispersion and interfacial coupling (Khan *et al.* 2024).

Dielectric loss (ε″) also increased with MgO loading, possibly because additional interfaces promoted charge-carrier accumulation, localized conduction, and polarization relaxation, as shown in Fig. 12(b). Dielectric loss represents electrical-energy dissipation rather than charge-storage capacity. Beyond an optimum concentration, extensive particle aggregation can interrupt uniform dispersion and alter the dielectric response. The observed results therefore support enhanced interfacial polarization following MgO incorporation. However, a higher dielectric constant accompanied by greater dielectric loss does not, by itself, confirm suitability for capacitors or energy-storage devices. Breakdown strength, loss tangent, conductivity, energy density, and cycling stability must also be evaluated. Sensor, coating, and electromagnetic-shielding applications would similarly require application-specific electrical and mechanical testing.

3.12 Photocatalytic Performance

Photocatalysis enables light-responsive materials to generate reactive species that can decompose organic contaminants. Antimicrobial activity cannot be claimed without separate microbial-inactivation experiments.

The photocatalytic behavior of the Chitosan–CMC/ZnO–MgO films was assessed using crystal violet (CV), as presented in Fig. 13. Fig. 13(a) shows that CV removal increased with irradiation time for every formulation. The Chitosan–CMC/ZnO reference film achieved approximately 25% removal, whereas the films containing 1%, 2%, and 3% MgO reached 31%, 42%, and 51%, respectively. The 3% formulation therefore produced the greatest final removal efficiency. The C/C_0 profiles in Fig. 13(b) similarly demonstrate a time-dependent decline in CV concentration, rather than MB, with faster removal after MgO incorporation.

Pseudo-first-order kinetic plots were constructed using $\ln(C_0/C)$ against irradiation, as illustrated in Fig. 13(c). Apparent rate constants were 0.0079, 0.0100, 0.0143, and 0.0125 min^{-1} for the Chitosan–CMC/ZnO, 1% MgO, 2% MgO, and 3% MgO films, respectively. The R^2 values near 0.99 indicate good agreement with the selected kinetic model. These rate constants do not increase continuously with MgO loading: k peaks at 2% MgO, while 3% provides the highest final removal efficiency. Fig. 13(d) confirms improved CV removal following MgO addition. Because the decrease in CV concentration can include adsorption, photocatalytic degradation should be distinguished using dark-adsorption and light-only control experiments.

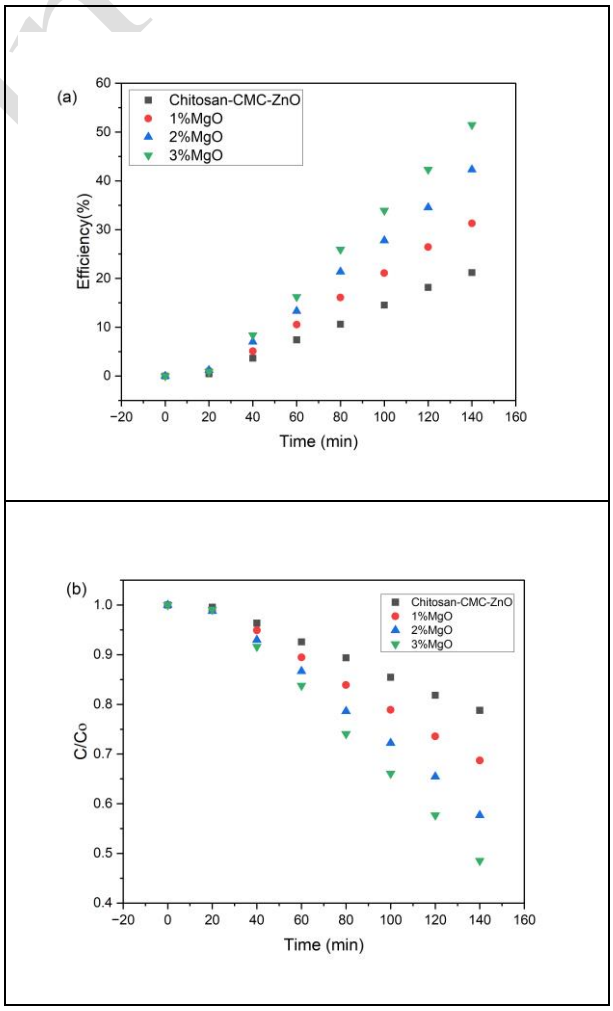

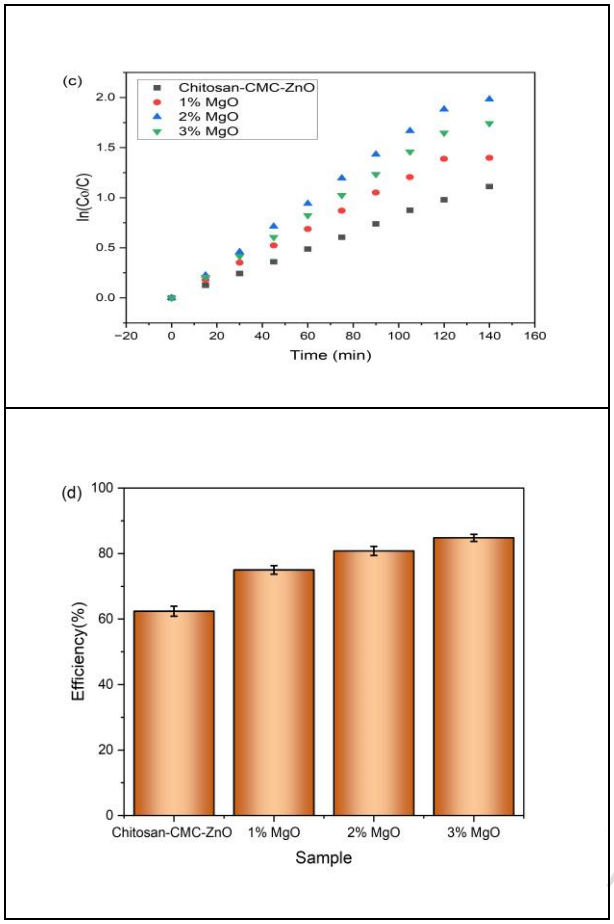

Fig. 13: (a) Degradation efficiency, (b) C/C_0 profiles, (c) degradation kinetics, and (d) final degradation efficiency comparison

The UV–Vis spectra exhibited a gradual decline in the characteristic absorption band of CV near 590 nm with increasing irradiation time, confirming progressive disruption of the dye chromophore. The reduction became more pronounced following MgO incorporation, particularly in the film containing 3 wt.% MgO. The enhanced photocatalytic response may be associated with improved charge separation at the ZnO–MgO interfaces and the subsequent production of ROS, including •OH and $•O_2^-$, which promote CV degradation.

After 140 min of UVA irradiation, the Chitosan–CMC/ZnO reference film achieved approximately 25% CV removal. Adding 1, 2, and 3 wt.% MgO increased the final removal efficiencies to 31%, 42%, and 51%, respectively. The apparent pseudo-first-order rate constants were 0.0079, 0.0100, 0.0143, and 0.0125 min^{-1} for the reference, 1%, 2%, and 3% MgO films, respectively. Thus, the 2 wt.% formulation exhibited the highest apparent reaction rate, whereas the 3 wt.% film produced the greatest final removal efficiency.

A previous investigation reported 97% CV degradation within 100 min under visible-light irradiation, compared with 60% for the corresponding unmodified photocatalyst (Muhiuddin *et al.* 2023). Differences in catalyst configuration, illumination source, dye concentration, and reaction conditions should be considered when comparing these results. Chitosan-stabilized MgO NPs have also demonstrated improved dispersion, surface stability, photocatalytic degradation, and antioxidant performance (Amor *et al.* 2024).

The moderate removal efficiency of the present films can be attributed to their immobilized configuration, in which part of the ZnO–MgO surface is embedded within the Chitosan–CMC matrix. Restricted dye diffusion, limited light penetration, mass-transfer resistance, and localized nanoparticle aggregation may reduce active-site accessibility. Nevertheless, the film configuration enables convenient catalyst recovery and minimizes post-treatment separation. Further studies could evaluate film thickness, porosity, ZnO/MgO ratio, catalyst leaching, degradation intermediates, mineralization efficiency, and repeated-use stability.

3.13 Antimicrobial Performance

Antimicrobial behavior is an important functional characteristic of nanocomposite films intended to inhibit microbial colonization and surface-associated growth. Their activity may involve disruption of cellular membranes, metal-ion release, and reactive oxygen species generation.

The antimicrobial effectiveness of the Chitosan–CMC/ZnO–MgO films was evaluated against Gram-positive *S. aureus*, Gram-negative *E. coli*, and the yeast *C. albicans* using a disc-diffusion assay. Fig. 14 presents the resulting inhibition zones. All tested formulations showed measurable antibacterial and antifungal activity, although inhibition varied among microorganisms. The Chitosan–CMC/ZnO reference film produced inhibition zones of 11.46 ± 0.38 mm against *E. coli*, 12.18 ± 0.42 mm against *S. aureus,* and 10.72 ± 0.35 mm against *C. albicans*.

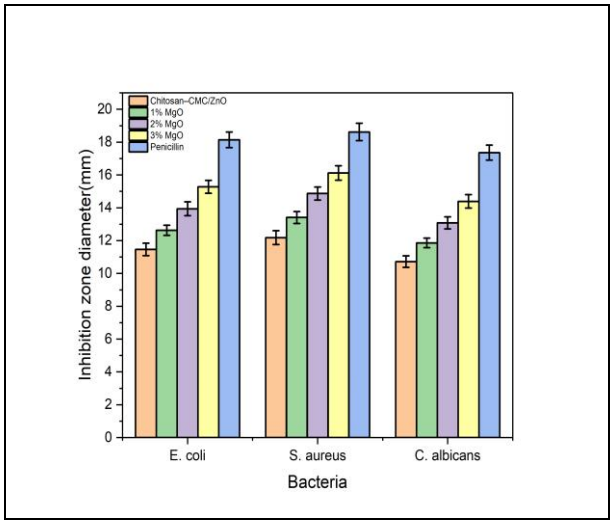

Fig. 14: Antimicrobial inhibition zones of the nanocomposite films

MgO incorporation significantly enhanced the antimicrobial activity of the Chitosan–CMC/ZnO films. Inhibition-zone diameters increased at 1 wt.% MgO and became more pronounced at 2 and 3 wt.%. The 3 wt.% MgO formulation produced the greatest inhibition zones: 16.12 ± 0.44 mm against *S. aureus*, 15.28 ± 0.39 mm against *E. coli*, and 14.39 ± 0.41 mm against *C. albicans*. These values demonstrate activity against Gram-negative and Gram-positive bacteria as well as the tested yeast under the applied disc-diffusion conditions.

A previous investigation reported inhibition zones of 21 ± 1.1 mm (approximately 96% inhibition) against *E. coli* and 30.1 ± 1.1 mm (approximately 99% inhibition) against *S. aureus* for nanoparticle-modified chitosan-coated fabrics (Ganvir *et al.* 2026). Although the present films produced smaller zones than the corresponding positive controls, the progressive increase following MgO incorporation confirms its contribution to antimicrobial performance.

The enhanced response may arise from the combined actions of chitosan, ZnO, and MgO. Chitosan can interact with negatively charged microbial surfaces and alter membrane permeability. ZnO may promote membrane disruption, Zn^{2+} release, and ROS formation, whereas MgO can induce alkaline stress, membrane damage, and oxidative injury. These processes may cause leakage of intracellular constituents and damage proteins and nucleic acids. Strong antimicrobial activity of chitosan–ZnO systems has similarly been associated with nanoparticle surface interactions, ion release, and cell-envelope disruption (Faisal *et al.* 2026).

Previous MgO-containing chitosan films achieved inhibition levels of 90.78% against *E. coli*, 88.83% against *S. aureus*, and 97.18% against *C. albicans* and demonstrated promising wound-healing properties (Mohamad *et al.* 2025). Differences in formulation, nanoparticle concentration, assay method, and microbial susceptibility should be considered when comparing these findings.

The greater activity of the Chitosan–CMC/ZnO–3 wt.% MgO film suggests a complementary contribution from the two metal oxides. However, confirmation of a true synergistic effect requires comparison with matched films containing ZnO or MgO individually. Moreover, disc-diffusion results depend on both antimicrobial potency and diffusion of active species in agar medium. Therefore, quantitative minimum inhibitory concentration, microbial reduction, nanoparticle leaching, cytocompatibility, and long-term stability tests are needed before considering these films for packaging, coating, or biomedical applications.

4. CONCLUSION

Chitosan–CMC/ZnO–MgO nanocomposite films were successfully fabricated and systematically evaluated. Structural characterization verified the cubic periclase phase of MgO and the incorporation of crystalline ZnO within the polymer matrix, while FT-IR findings indicated interfacial interactions among chitosan, CMC, ZnO, and MgO. MgO addition improved thermal resistance, increasing the apparent activation energy from 86 to 122 kJ mol^{-1} and the glass-transition temperature from 98.5 to 117 °C. These changes suggest restricted segmental mobility within the polymer network.

Mechanical performance also improved with MgO loading. Tensile strength increased from 28.6 to 51.6 MPa, while Shore A hardness rose from 41.8 to 62.7, demonstrating the reinforcing contribution of MgO. Contact-angle measurements indicated a transition toward a more hydrophobic surface, with the water contact angle increasing from 71.26° to 93.17°. The dielectric constant increased after MgO incorporation, reflecting changes in interfacial polarization and charge-transport behavior.

Photocatalytic testing showed that crystal violet removal increased from 25% for the Chitosan–CMC/ZnO reference film to 51% for the 3 wt.% MgO formulation. Antimicrobial assays showed improved activity against *E. coli*, *S. aureus*, and *C. albicans*, with inhibition zones of 14.39, 16.12, and 15.28 mm, respectively, for the 3 wt.% MgO formulation, suggesting complementary contributions from chitosan, ZnO, and MgO. Overall, MgO incorporation enhanced the mechanical, thermal, electrical, surface, antimicrobial, and photocatalytic characteristics of the films.

The present investigation did not assess cellular compatibility, cytotoxicity, hemocompatibility, or the release of nanoparticles or ions. Consequently, findings establish material functionality but do not demonstrate biomedical safety. Further studies could examine these parameters, along with photocatalytic reusability and environmental stability, before considering application-specific use.

FUNDING

This research received no specific grant from any funding agency in the public, commercial, or not-for-profit sectors.

CONFLICTS OF INTEREST

The authors declare that there is no conflict of interest.

COPYRIGHT

REFERENCES

Abdeltwab, E., Atta, A., Al-Harbi, N. and Abdelhamied, M. M., Synthesis, characterization and dielectric properties of polymer nanocomposites for energy storage applications, *Macromol. Res.*, 32(11), 1113–1122 (2024). https://doi.org/10.1007/s13233-024-00298-y

Alamdari, S., Mirzaee, O., Nasiri Jahroodi, F., Tafreshi, M. J., Ghamsari, M. S., Shik, S. S., Ara, M. H. M., Lee, K. Y. and Park, H. H., Green synthesis of multifunctional ZnO/chitosan nanocomposite film using wild Mentha pulegium extract for packaging applications, *Surf. Interf.*, 34, 102349(2022). https://doi.org/10.1016/j.surfin.2022.102349

Al-Odayni, A. B., Saeed, W. S. and Abdu, N. A. Y., Phyto-mediated synthesis of ZnO NPs using guava leaf extract: characterization, antibacterial activity, and hemolysis effect, *Biomass Convers. Biorefine.*, 14(20), 26149–26157 (2024). https://doi.org/10.1007/s13399-023-04683-y

Amor, I. Ben, Hemmami, H., Laouini, S. E., Ahmed, S., Mohammed, H. A., Abdullah, J. A. A., Azooz, E. A., Al-Mulla, E. A. J. and Alharthi, F., Enhancing oxidant and dye scavenging through MgO-based chitosan nanoparticles for potential antioxidant coatings and efficient photocatalysts, *Biomass Convers. Biorefine.*, 14(24), 32343–32357 (2024). https://doi.org/10.1007/s13399-023-04923-1

Attayil, S. S., Kalimuthu, B., Selvamurugan, N. and Mani, P., Wound dressings based on chitosan/gelatin/MgO composite films, *Int. J. Polym. Mater. Polym. Biomater.*, 71(16), 1252–1261 (2022). https://doi.org/10.1080/00914037.2021.1960342

Bisht, R., Joshi, G. C. and Joshi, C. S., Investigation of the effect of Cu doping on dielectric and photocatalytic behaviour of SnO_2 nanoparticles, *J. Mater. Sci. Mater. Electron.*, 36(4), 235(2025). https://doi.org/10.1007/s10854-025-14288-y

Ebenezer, A. J. P., Caroline, A. L., Mayakannan, S., Dhivya, M., Sri, T. S. and Saravanan, V., Optimization of Green-synthesized Graphene Quantum Dots using Machine Learning for Neuroprotective Antioxidant Applications, *J. Environ. Nanotechnol.*, 15(2), 463–478 (2026). https://doi.org/10.13074/jent.2026.06.2622142

Faisal, M., Rosyidah, H., Khadarsih, S. and Desvita, H., Characterization of chitosan-based edible coatings enriched with oil palm empty fruit bunch liquid smoke and neem extract, *J. Eco. Eng.*, 27(4), 131–142 (2026). https://doi.org/10.12911/22998993/214813

Ganvir, V. Y., Satishkumar, P., Awachat, D. B., Rani, A., Talodhikar, V. and Krishnaraj, C., Biofabricated CuO Nanoparticle Reinforced Bamboo Fiber Coatings for Photocatalytic Antimicrobial and Superhydrophobic Biomedical Textile Applications, *J. Environ. Nanotechnol.*, 15(2), 330–343 (2026). https://doi.org/10.13074/jent.2026.06.2622243

Ghanbari, E., Khazaei, M., Mehdipour, A., Khoshfetrat, A. B. and Niknafs, B., Green Synthesized Magnesium Oxide Nanoparticles Reinforce Osteogenesis Properties of Bacterial Cellulose Scaffolds for Bone Tissue Engineering Applications: An In Vitro Assessment, *Cell J.*, 25(7), 483–495 (2023). https://doi.org/10.22074/CELLJ.2023.1986179.1204

Guan, G., Zhang, L., Zhu, J., Wu, H., Li, W. and Sun, Q., Antibacterial properties and mechanism of biopolymer-based films functionalized by CuO/ZnO nanoparticles against *Escherichia coli* and *Staphylococcus aureus*, *J. Hazard. Mater.*, 402, 123542(2021). https://doi.org/10.1016/j.jhazmat.2020.123542

Huang, S., Liu, H., Song, W., Zhang, C., Zhang, Z. and Yao, C., Integrated monitoring and preservation of freshness: CMC/Anth/GNPs/CS multifunctional intelligent film for shrimp packaging, *Europe. Food Res. Technol.*, 252(3), 124(2026). https://doi.org/10.1007/s00217-026-05090-z

Huong, N. T., Son, N. N., Thanh, V. M. and Ha, N. D., Glutamic acid–coated zinc oxide nanoparticles: synthesis, characterization, and anticancer activity, *J. Nanopart. Res.*, 27(1), 15(2025). https://doi.org/10.1007/s11051-024-06206-w

Jachak, S. R., Srinivasan, R., Arunkumar, S., Kumar, V. N., Manu, Y. M. and Mayakannan, S., Development of MUF-bonded Banyan Fiber Laminates Reinforced with Bio-synthesized CeO_2 Nanoparticles for Advanced Applications, *J. Enviro. Nanotechnol.*, 15(2), 554–562 (2026). https://doi.org/10.13074/jent.2026.06.2622149

Kamanna, K., Amaregouda, Y. and N, M. K., Chitosan/polyvinyl alcohol-based nanocomposite films incorporated with L-Glu surface functionalized ZnO NPs: Physicochemical, photocatalytic, antimicrobial and antioxidant properties evaluation, *Environ. Nanotechnol. Monitor. Manage.*, 20, 100861(2023). https://doi.org/10.1016/j.enmm.2023.100861

Karabaş, E., Yurddaskal, M., Bozatlı, S. B. and Yılmaz, T., Production of zinc oxide (ZnO) doped biodegradable film and investigation of its photocatalytic/antimicrobial properties, *J. Photochem. Photobio. A: Chem.*, 462, 116214(2025). https://doi.org/10.1016/j.jphotochem.2024.116214

Kashyap, D. N., Shalom, N., Mayakannan, S., Muthuraj, M., Thanikasalam, A. and Ahmed, A. A,. Comparative Green and Wet-chemical Synthesis of ZnO Nanoparticles: Enhanced Photocatalytic and SERS Performance of Defect-rich Nanostructures, *J. Environ. Nanotechnol.*, 15(2), 162–175 (2026). https://doi.org/10.13074/jent.2026.06.2612090

Khalid, S. A., Ghanem, A. F., Abd-El-Malek, A., Ammar, M. A., El-khateib, T. and El-Sherbiny, I. M., Free-standing carboxymethyl cellulose film incorporating nanoformulated pomegranate extract for meat packaging, *Carbohydrate Polym.*, 332, 121915(2024). https://doi.org/10.1016/j.carbpol.2024.121915

Khan, A. U. R., Khan, S. U. R., Al-Mohaimeed, A. M., Al-onazi, W. A., Chen, T. W. and Imran, M., Green mediated approach to investigate the optical, structural, photocatalytic, magnetic and dielectric properties of Cr^{3+} doped ZnO nanoparticles for energy applications, *Ceram. Int.*, 50(21), 42809–42817 (2024). https://doi.org/10.1016/j.ceramint.2024.08.126

Li, B., Li, F., Cai, S., Tang, T., Chen, H., Feng, K. and Bai, Y., Tea Polyphenol–Loaded Chitosan Nanoparticles Incorporated into Carboxymethyl Cellulose/Potato Starch to Develop Sustained-Release Bioactive Films for Pork Preservation, *Packaging Technol. Sci.*, 39(2), 161–180 (2026). https://doi.org/10.1002/pts.70027

Losetty, V., Devanesan, S., AlSalhi, M. S., Velu, P. P., Muthupillai, D., Kumar, K. A. and Lakkaboyana, S. K., Green synthesis of silver nanoparticles using Malachra alceifolia (wild okra) for wastewater treatment and biomedical applications with molecular docking approach, *Environ. Sci. Pollut. Res.*, 31(43), 55562–55576 (2024). https://doi.org/10.1007/s11356-024-34872-9

Ma, W., Zhang, Y., Chen, L., Xie, X., Yuan, S., Qiu, Z., Zhu, G. and Guo, J., A novel ZnO-TiO2-Bi_2WO_6/Carboxymethyl chitosan composite with high antimicrobial activity and visible-light catalytic degradation of ethylene towards banana preservation in hot and humid environments, *Int. J. Bio. Macromol.*, 281, 136559(2024). https://doi.org/10.1016/j.ijbiomac.2024.136559

Mathew, D., Thomas, B., Sudheep, N. M., Varghese, S., Yesudas, V., Thomas, J. B. and Radhakrishnan, E. K., Psidium guajava Leaf Phytochemical-Assisted One-Step Synthesis of Metformin/ZnO Nanoconjugate for Enhanced Solubility, Hydrophilicity, Biocompatibility, and Broad-Spectrum Therapeutic Potential, *J. Clust. Sci.*, 37(4), 100(2026). https://doi.org/10.1007/s10876-026-03057-4

Mohamad, E. A., Gad, A. M., Abd El-Rhman, R. H., Moselhey, M. T. H. and Madian, N. G., Dressing membrane composites of PVA/chitosan/MgO nanoparticles for wound healing applications in rat model, *Naunyn-Schmiedeberg's Archives Pharmacol.*, 398(6), 6989–7003 (2025). https://doi.org/10.1007/s00210-024-03716-1

Mohamad, E. A., Shehata, A. M., Abobah, A. M., Kholief, A. T., Ahmed, M. A., Abdelhakeem, M. E., Dawood, N. K. and Mohammed, H. S., Chitosan-based films blended with moringa leaves and MgO nanoparticles for application in active food packaging, *Int. J. Bio. Macromol.*, 253, 127045(2023). https://doi.org/10.1016/j.ijbiomac.2023.127045

Mohammadi, H., Rezaeigolestani, M. and Mohsenzadeh, M., Optimization of antimicrobial nanocomposite films based on carboxymethyl cellulose incorporating chitosan nanofibers and Guggul gum polysaccharide, *Sci. Rep.*, 14(1), 13693(2024). https://doi.org/10.1038/s41598-024-64528-0

Muhiuddin, G., Bibi, I., Nazeer, Z., Majid, F., Kamal, S., Kausar, A., Raza, Q., Alwadai, N., Ezzine, S. and Iqbal, M., Synthesis of Ni-doped barium hexaferrite by microemulsion route to enhance the visible light-driven photocatalytic degradation of crystal violet dye, *Ceram. Int.*, 49(3), 4342–4355 (2023). https://doi.org/10.1016/j.ceramint.2022.09.319

Pham, T. T., Lieu, L., Nguyen, A. T. and Le, T. T. T., Chitosan films integrated with zinc oxide/reduced graphene oxide nanocomposite for malachite green degradation and antibacterial activity in sustainable packaging, *Int. J. Bio. Macromol.*, 318, 145009(2025). https://doi.org/10.1016/j.ijbiomac.2025.145009

Rajendran, N. K., George, B. P., Houreld, N. N. and Abrahamse, H., Synthesis of zinc oxide nanoparticles using rubus fairholmianus root extract and their activity against pathogenic bacteria, *Mol.*, 26(10), 3029(2021). https://doi.org/10.3390/molecules26103029

Sangodkar, V., Vaidya, M., Ayyanar, M., Prabhu, S., Nadaf, S., Naik, A. V, Gurav, N., Kumbhar, P., Kharkar, P. and Gurav, S., Biopolymeric chitosan/ZnO-nanocomposite films from pomegranate peels for sustainable and functional food packaging, *Inorg. Chem. Commun.*, 186, 116200(2026). https://doi.org/10.1016/j.inoche.2026.116200

Thungphotrakul, N. and Prapainainar, P., Development of polyvinyl alcohol/carboxymethylcellulose-based bio-packaging film with citric acid crosslinking and clove essential oil encapsulated chitosan nanoparticle pickering emulsion, *Int. J. Bio. Macromol.*, 282, 137223 (2024). https://doi.org/10.1016/j.ijbiomac.2024.137223

Vaikundam, M., Santhanam, A. and Narenkumar, J., Halloysite-enriched pectin-capped ZnO nanoparticles as a bioplastic nanocomposite film, *J. Indian Chem. Soc.*, 103(5), 102555(2026). https://doi.org/10.1016/j.jics.2026.102555

Valsalan, A., Paramasivan, S., Nagarajan, R., Ayrilmis, N., Krishnan, K. and Mohammad, F., Biodegradable Hybrid Films from Cellulose Nanocrystals and

Chitosan Reinforced with Nano-Magnesium Oxide/Neem Oil for Enhancing Packaging Performance, *J. Appl. Polym. Sci.*, 143(6), e70002(2026). https://doi.org/10.1002/app.70002

Yang, J., Wang, X., Khan, M. R., Hammouda, G. A., Alam, P., Meng, L., Zhang, Z. and Zhang, W., New opportunities and advances in magnesium oxide (MgO) nanoparticles in biopolymeric food packaging films, *Sustain. Mater. Technol.*, 40, e00976(2024). https://doi.org/10.1016/j.susmat.2024.e00976